

Research Article

Genesis of the Longmendian Ag–Pb–Zn Deposit in Henan (Central China): Constraints from Fluid Inclusions and H–C–O–S–Pb Isotopes

Xinglin Chen,^{1,2,3} Yongjun Shao,^{2,3} Chunkit Lai,⁴ and Cheng Wang^{2,3} 

¹School of Resources and Safety Engineering, Central South University, Changsha 410083, China

²Key Laboratory of Metallogenic Prediction of Non-Ferrous Metals and Geological Environment Monitoring (Central South University), Ministry of Education, Changsha 410083, China

³School of Geosciences and Info-Physics, Central South University, Changsha 410083, China

⁴Faculty of Science, Universiti Brunei Darussalam, Gadong BE1410, Brunei Darussalam

Correspondence should be addressed to Cheng Wang; csuwangcheng@csu.edu.cn

Received 18 August 2019; Revised 16 June 2020; Accepted 25 June 2020; Published 13 July 2020

Academic Editor: Micòl Mastroicco

Copyright © 2020 Xinglin Chen et al. This is an open access article distributed under the Creative Commons Attribution License, which permits unrestricted use, distribution, and reproduction in any medium, provided the original work is properly cited.

The Longmendian Ag–Pb–Zn deposit is located in the southern margin of the North China Craton, and the mineralization occurs mainly in quartz veins, altered gneissic wallrocks, and minor fault breccias in the Taihua Group. Based on vein crosscutting relations, mineral assemblages, and paragenesis, the mineralization can be divided into three stages: (1) quartz–pyrite, (2) quartz–polymetallic sulfides, and (3) quartz–carbonate–polymetallic sulfides. Wallrock alteration can be divided into three zones, i.e., chlorite–sericite, quartz–carbonate–sericite, and silicate. Fluid inclusions in all Stage 1 to 3 quartz are dominated by vapor–liquid two-phase aqueous type (W-type). Petrographic and microthermometric analyses of the fluid inclusions indicate that the homogenization temperatures of Stages 1, 2, and 3 are 198–332°C, 132–260°C, and 97–166°C, with salinities of 4.0–13.3, 1.1–13.1, and 1.9–7.6 wt% NaCl_{eqv}, respectively. The vapor comprises primarily H₂O, with some CO₂, H₂, CO, N₂, and CH₄. The liquid phase contains Ca²⁺, Na⁺, K⁺, SO₄²⁻, Cl⁻, and F⁻. The sulfides have $\delta^{34}\text{S} = -1.42$ to $+2.35\%$ and $^{208}\text{Pb}/^{204}\text{Pb} = 37.771$ to 38.795, $^{207}\text{Pb}/^{204}\text{Pb} = 15.388$ to 15.686, and $^{206}\text{Pb}/^{204}\text{Pb} = 17.660$ to 18.101. The H–C–O–S–Pb isotope compositions indicate that the ore-forming materials may have been derived from the Taihua Group and the granitic magma. The fluid boiling and cooling and mixing with meteoric water may have been critical for the Ag–Pb–Zn ore precipitation. Geological and geochemical characteristics of the Longmendian deposit indicate that the deposit is best classified as medium- to low-temperature intermediate-sulfidation (LS/IS) epithermal-type, related to Cretaceous crustal-extension-related granitic magmatism.

1. Introduction

The Longmendian Ag–Pb–Zn deposit is located in the Shagou (Xiayu) orefield of the Xiong'er region (western Henan Province) in central China. Tectonically, the deposit is located at the southern margin of the North China Craton (NCC), bordered with the eastern Qinling–Dabie Orogen. The NCC is one of the world's oldest craton, with a history dating back to >3.8 Ga. It is also an important mineral province, hosting a variety of ore deposits [1, 2]. The Mesozoic granites and hydrothermal mineralization systems in the Xiong'er region (southern NCC margin) have been widely

studied [3–11]. The regional Au and Mo mineralization was coeval with the first Mesozoic magmatic phase there (late Jurassic–early Cretaceous, ca. 158–136 Ma), which was related to the Paleo-Pacific plate subduction beneath Eastern China [1]. Meanwhile, Ag–Pb–Zn mineralization was mostly coeval with the second magmatic phase (early Cretaceous, ca. 134–108 Ma) [12–14], which is related to lithospheric thinning–asthenospheric upwelling caused by the subduction-direction change of the Paleo-Pacific Plate [1, 2]. In addition, Neoproterozoic Mo mineralization was also reported locally, as represented by the Zhaiao and Longmendian deposits [15, 16].

The Longmendian Mo mineralization is spatially related to the migmatites but distal from intrusions or faults [17]. Four types of fluid inclusions (FIs) have been recognized in the Mo-bearing quartz and calcite grains, i.e., $\text{CO}_2 \pm \text{CH}_4$ -bearing FIs (PC-type), CO_2 - H_2O -bearing FIs (C-type), daughter mineral-bearing FIs (S-type) and H_2O - NaCl FIs (W-type). The ore fluid temperature and pressure were estimated to be around 225 to 390°C and 114 to 265 MPa, respectively [17]. Geological and FI features indicate that the Mo mineralization, which was molybdenite Re-Os dated to be 1875 Ma, was caused by the high temperature migmatitic fluid/melt [15–17]. The Paleoproterozoic mineralization event was interpreted to have linked to the collision between the western and eastern NCC along the Trans North China Orogen at 1.85 Ga [15, 16].

Meanwhile, Longmendian Ag-Pb-Zn mineralization is of a much larger scale than the Mo mineralization. The relationship between the Ag-Pb-Zn and Mo mineralization, as well as their respective ore material/fluid source and metallogenesis, remains unclear. In this study, therefore, we addressed these issues via FI microthermometric and H-O-C-S-Pb isotope analyses.

2. Regional Geology

The Xiong'er terrane is an important part of the Kunlun-Qinling-Dabie Orogen. The terrane, encompassing an area of 80 km long (E-W) and 15 km wide (N-S), is bound by the EW-trending Machaoying fault in the south and the Luoning fault in the north (Figure 1). Prolonged and multiphase intensive orogenic events have controlled the formation of the structural framework, magmatism, and sedimentation of the region, with consequently influenced the Xiong'er metallogeny. The regional tectonic events include the formation of the continental nucleus and then the cratonic basement in the Paleoproterozoic, Mesoproterozoic rifting, Neoproterozoic-to-Paleozoic sedimentation, and Mesozoic tectonic reactivation. The study area is located in the western Xiong'er (Figure 1).

Local stratigraphy is characterized by crystalline basement with metavolcanic-sedimentary cover. The crystalline basement is primarily composed of the Neoproterozoic Taihua Group (Gp) metamorphosed terrane, while the metavolcanic-sedimentary cover is composed of Mesoproterozoic Xiong'er Group (Gp.) low-grade metavolcanic rocks. The Taihua Group in the study area strikes ENE and is dominated by biotite/amphibole plagioclase interlayered with (plagioclase) amphibolite, granulite, and leptyte. Regionally, the Xiong'er Gp. volcanic rocks overlie the Taihua Group along an unconformity, which was formed by the 1.85 Ga collision between the eastern and western NCC. The rock types of the Xiong'er Gp. consist of mainly (pyroxene) andesite porphyry with local siltstone-mudstone/shale interbeds.

Local structure is controlled by a series of NE-trending detachment faults along/around a metamorphic core complex, the most important of which lies on the unconformity between the Xiong'er Group and Taihua Group (Figure 2). The main detachment fault and the NE-trending shears are the major Ag-Pb-Zn ore-hosting structures [20]. Local folds

include mainly the EW-trending recumbent-overtaken folds and the NS-trending anticlines and synclines. The Machaoying fault is the major regional fault and is located in the southern Xiong'er. Faults/fractures are well developed in the study area and are mainly NE-trending and minor NW-trending and NS-trending. NE-trending structures are the main ore host.

In the study area, the widely exposed magmatic rocks were mainly formed in the Archean, Mesoproterozoic, and Mesozoic: Archean magmatic rocks include mafic to felsic volcanic rocks and late-stage ultramafic intrusions (e.g., dykes). The rocks are metamorphosed into gneiss, plagioclase amphibolite, and migmatite; Mesoproterozoic magmatic rocks comprise extensive intermediate-mafic volcanic rocks (ca. 1780–1320 Ma [21]) and the Xiong'er diorite in Songxian County (zircon U-Pb age: 1440 Ma [22]); Mesozoic magmatic rocks are widespread and multiphase. Their formation was primarily restricted largely to the Yanshanian (Jurassic-Cretaceous), although Indosinian (Triassic) one is also reported [23]. The Yanshanian magmatic rocks are mostly granite batholiths and minor granite stocks and medium-felsic dykes. Furthermore, numerous outcrops of small-sized explosive-breccias are observed and generally regarded to be closely ore-related [23]. The granite batholiths are distributed mainly in the eastern Xiong'er, e.g., the Huashan, Jinshanmiao, Wuzhangshan, and Heyu intrusions. Previous works indicated that Yanshanian magmatism may have facilitated extensive migration of metallogenic materials along/across the sequences and that the postmagmatic hydrothermal fluids constitute an important component of the ore fluids [24].

3. Deposit Geology

The Longmendian deposit is located to the west of the Xiong'er metamorphic core complex (Figure 3). The exposed metamorphosed sequences comprise primarily the Neoproterozoic Taihua Group and the Mesoproterozoic Xiong'er Group. The Taihua Group is distributed to the north of Longmendian and comprises dominantly biotite plagioclase gneiss and migmatized amphibole-plagioclase gneiss. The sequence is underlain by numerous amphibolite bodies. The Xiong'er Group is distributed to the southeast of Longmendian and comprises mainly andesite, particularly pyrite-bearing amygdaloidal and porphyritic ones. Andesitic rocks at Longmendian are generally altered, with the plagioclase strongly sericitized and the groundmass chlorite- and epidote-altered.

At Longmendian, detachment faults and secondary NE faults are the dominating structures, whereas folds are not well developed. The detachment faults strike NE with dip angles of 20–35°. The unconformity interface between the Taihua Group and Xiong'er Group is overprinted by slickensides of the detachment faults. The NE-trending (NW-dipping) faults, tectonic breccia, and mylonites are commonly altered. Magmatic rocks include mainly diabase and few ultramafic rocks. The diabase intruded into the Taihua Gp. sequence in the form of near-vertical dykes. The major minerals include pyroxene and plagioclase. The plagioclase phenocrysts (5–10 vol%) are commonly sericite-

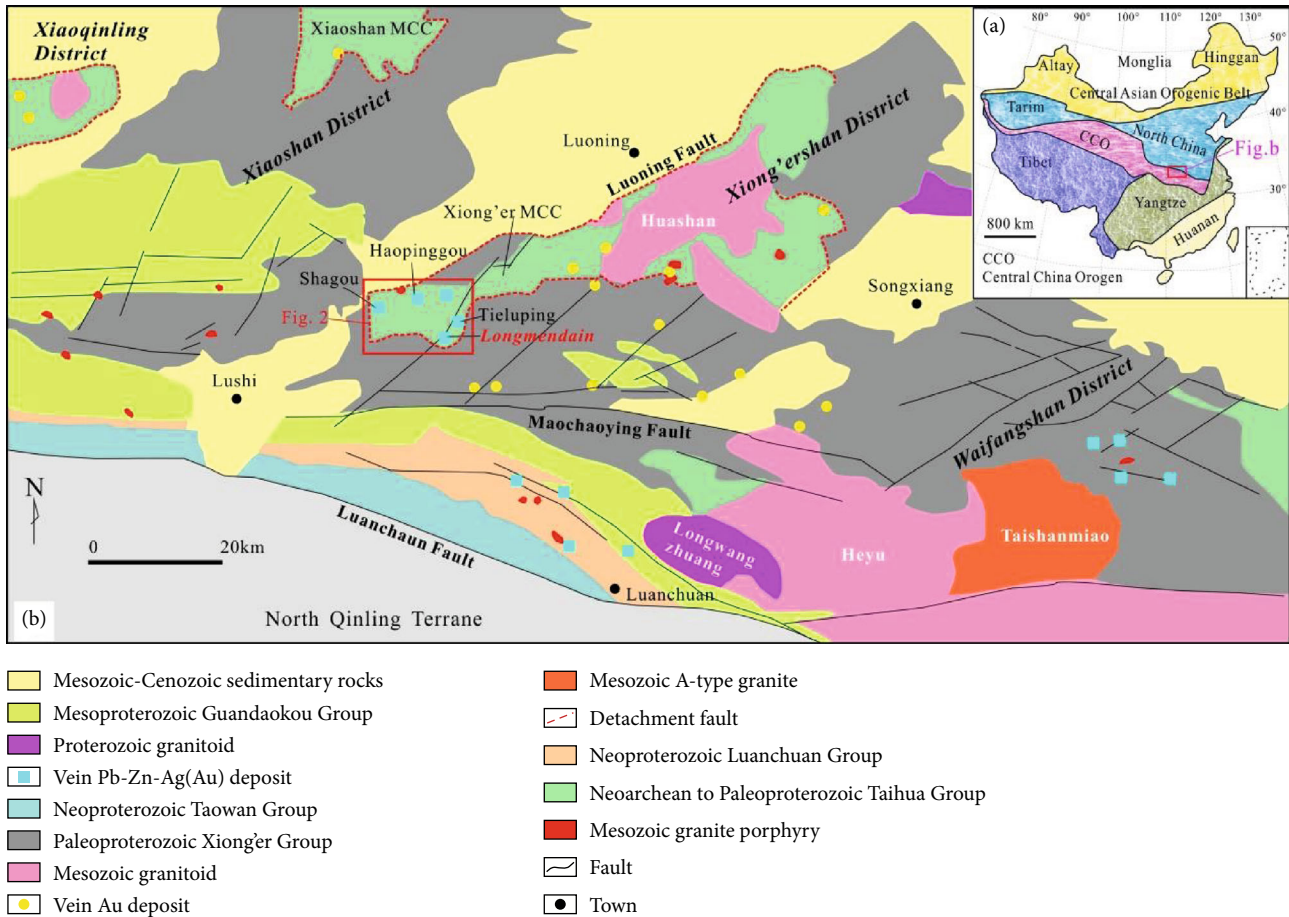


FIGURE 1: Location and regional geology of the East Qinling Orogen. (a) Tectonic framework of China, showing the location of Qinling Orogen. (b) Regional geologic map of the Xiong'er terrane, showing the location of the Shagou Ag-Pb-Zn ore field. MCC: metamorphic core complex (modified from [18, 19]).

and epidote-altered, while the pyroxenes are generally altered to actinolite. Accessory minerals include ilmenite, magnetite, apatite, zircon, and ilmenite. Ultramafic dykes (100 m long and 10 m wide) are locally exposed to the north of Longmendian.

The orebodies are mainly of quartz vein and altered-rock types (Figure 4). Metallic minerals include primarily galena and sphalerite, followed by pyrite, chalcopyrite, Ag-bearing tetrahedrite, pyrargyrite, argyrite, polybasite, native Ag, tetrahedrite, and bornite. Nonmetallic minerals include primarily quartz, calcite, siderite, ankerite, fuchsite, and sericite, followed by feldspar, chlorite, amphibole, biotite, and apatite (Figure 4). Ore structures include mainly massive, vein/stockwork, banded, brecciated, and disseminated, while ore textures include (hyp)idiomorphic, xenomorphic granular, skeletal, rimmed, and zoned (Figure 4). Alteration types include silicic, sericite, chlorite, carbonate, and pyrite. Ore proximal wallrock alterations are dominated by silicic and sericite, and locally weak potassic feldspar, while the ore distal ones include mainly chlorite and carbonate.

Three alteration zones were identified according to the alteration minerals and their assemblage (Figure 5):

- (1) Chlorite-sericite zone: this zone is developed on the periphery of the fractured zone. Altered feldspars,

hydrothermal quartz, carbonate veinlets, and few galena veinlets are observed in this zone, and alteration intensity is commonly low.

- (2) Quartz-calcite-dolomite-sericite zone: this zone is developed within the fracture zone and is characterized by varying widths and ore wallrock interlayers. This stage is mostly associated with Ag mineralization.
- (3) Silicic zone: this zone is located at the center of the fractured zone and is the mineralization center and the most altered part. The altered rocks are primarily composed of quartz and sulfides. Concentrations of Si and K tend to increase while that of Na decreases from the fresh wallrock to the silicic core, which corresponds to increasing quartz and sericite but decreasing sodic feldspar contents, respectively, by wallrock alteration.

Mineralization is divided into three stages according to spatial distributions and vein crosscutting relationships (Figure 6):

- (1) Quartz-pyrite stage: this stage is dominated by silicification and formed allotriomorphic granular quartz. Alteration minerals, such as sericite, fuchsite, and few vein/disseminated pyrites, are also observed. Quartz

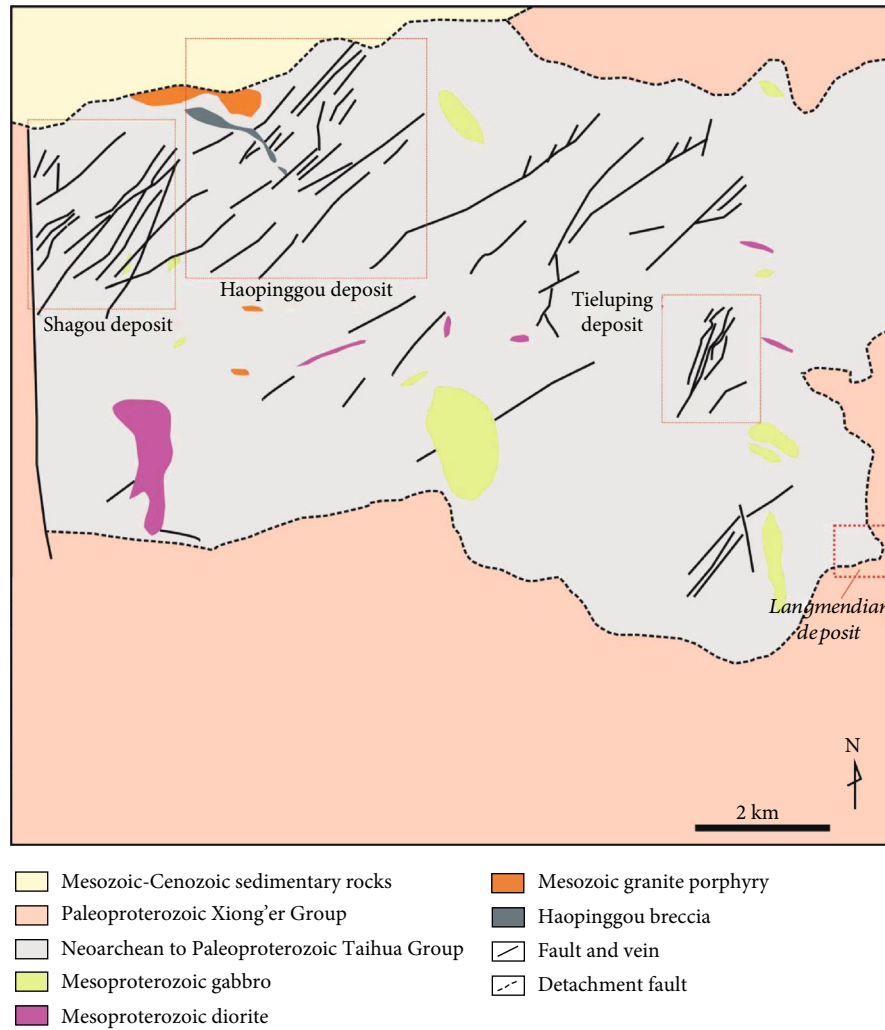


FIGURE 2: Geologic map of the Shagou (Xiayu) Ag-Pb-Zn ore field (modified from [18]).

and pyrite show cataclastic texture and are associated with metallic minerals from the late Ag ore period.

- (2) Quartz-polymetallic sulfide stage: this stage represents the main Ag-Pb-Zn ore stage and has a wide variety of metallic minerals including galena, sphalerite, pyrite, chalcopyrite, (Ag-bearing)-tetrahedrite, sulfosalts, and native Ag. Galena, sphalerite, and Ag sulfides are associated with sulfosalts and occur within the fracture-infilling veins.
- (3) Quartz-carbonate-polymetallic sulfide stage: hydrothermal minerals include mainly calcite, dolomite, ankerite and siderite, and, locally, quartz, pyrite, and chalcopyrite. Furthermore, carbonate (calcite and dolomite) druses and geodes are often observed.

4. Sampling and Analysis Methods

4.1. Sampling. Doubly polished thin sections were made from 19 quartz and 6 calcite samples associated with the three ore stages (Figure 3). 11 samples for H-O isotope analysis and 26

samples for C-O isotope analysis were selected under the microscope to ensure that they represent all Stages 1 to 3, and all the samples were crushed and ground into 40–80 mesh granules. 26 and 28 representative samples were selected for sulfur and lead isotope analyses, respectively. The samples were milled into 200 mesh.

4.2. Fluid Inclusions. Petrographic observations and temperature measurements of fluid inclusions (FIs) were made with a Linkam THMSG600 heating-freezing stage at the Key Laboratory of Metallogenic Prediction of Nonferrous Metals and Geological Environment Monitoring (Central South University). Analytical precisions were than $\pm 1^\circ\text{C}$ and $\pm 0.1^\circ\text{C}$ for temperatures of 30 to 600°C and -196 to 30°C , respectively. Freezing and heating temperatures were measured using the same inclusions (where possible), and phase transitions were carefully monitored. The temperatures were initially modified by steps of $5^\circ\text{C}/\text{min}$ and changed gradually by steps of $0.2^\circ\text{C}/\text{min}$ when approaching the phase transition.

Bulk FI analysis was performed for the gas-liquid-phase compositions at single mineral purity $> 89\%$. The analysis was conducted at the same laboratory with a Varian-3400

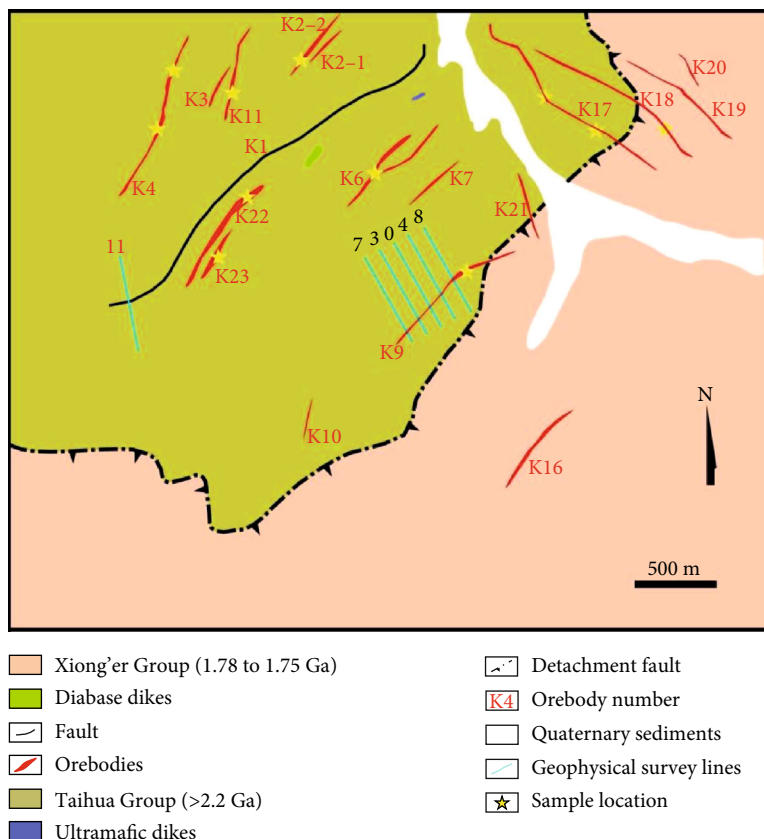


FIGURE 3: Geologic map of the Longmendian Ag-Pb-Zn deposit.

gas chromatograph (Varian) and a DX-120 ion chromatograph (Dionen). The analytical error was less than 5%.

4.3. Hydrogen-Oxygen Isotope Analyses. The H-O isotope samples were collected from the drill core. Eight mineral samples representing different stages were selected for the analyses. The samples were approximately 20 mesh with a purity of ~99.5%. Vacuum thermal explosion and zinc reduction methods were adopted to extract the hydrogen. The BrF_5 method was used to obtain pure O_2 from quartz samples (under vacuum conditions; at 500–680°C), which was subsequently transferred into CO_2 . The H-O isotope analyses were conducted at the BRIUG (Beijing Research Institute of Uranium Geology) Analytical Laboratory with a MAT-253 mass spectrometry. Analytical errors for the H and O isotope analyses are 0.2 and 2‰, respectively.

4.4. Carbon-Oxygen Isotope Analyses. Calcite C-O isotope compositions were obtained using the MAT-251 EM mass spectrometer at the BRIUG Analytical Laboratory. Calcite reacts with pure phosphoric acid to produce CO_2 . The analytical precisions (2σ) are $\pm 0.2\text{‰}$ for carbon isotope and $\pm 2\text{‰}$ for oxygen isotope. C-O isotope compositions are reported relative to PDB ($\delta^{18}\text{O}_{\text{SMOW}} = 1.03086 \times \delta^{18}\text{O}_{\text{PDB}} + 30.86$).

4.5. Sulfur-Lead Isotope Analyses. The isotope samples were collected from both open pits and drill cores. Pure single minerals (>95%) were selected for isotope analyses. Cu_2O

was used as an oxidizing agent for the sulfide sample to produce SO_2 , which was subsequently frozen and collected for the S isotope analysis with a MAT-251 mass spectrometer. The international standard V_{CDT} was used in this regard, and the accuracy is $\pm 2\text{‰}$. The Pb isotope analyses were conducted with an IsoProbe-T thermal ionization mass spectrometer. Lead was separated and purified using the conventional cation-exchange technique (with diluted HBr as the eluant). The $^{208}\text{Pb}/^{206}\text{Pb}$, $^{207}\text{Pb}/^{206}\text{Pb}$, and $^{204}\text{Pb}/^{206}\text{Pb}$ ratios of the NBS981 Pb standard were 2.1681 ± 0.0008 (2σ), 0.91464 ± 0.00033 (2σ), and 0.059042 ± 0.000037 (2σ), respectively. The analyses were conducted at the BRIUG Analytical Laboratory.

5. Results

5.1. Fluid Inclusions

5.1.1. Morphology. Abundant FIs are trapped in the quartz from Stage 1 to Stage 3 carbonate-quartz veins. These isolated/randomly clustered FIs in the quartz crystals are interpreted as primary ([25]; Figures 7(d)–7(h)). The FIs (from Stage 1 to Stage 3) are dominantly vapor-liquid two-phase aqueous (W) type (Figure 7). W-type FIs are composed of gas and liquid phases at room temperature. Individual FIs are 10–30 μm large with a filling percentage of 10–90%. The inclusions are dominantly irregular in shape, followed by ellipsoidal, elongated, and lentoid, with locally rectangular

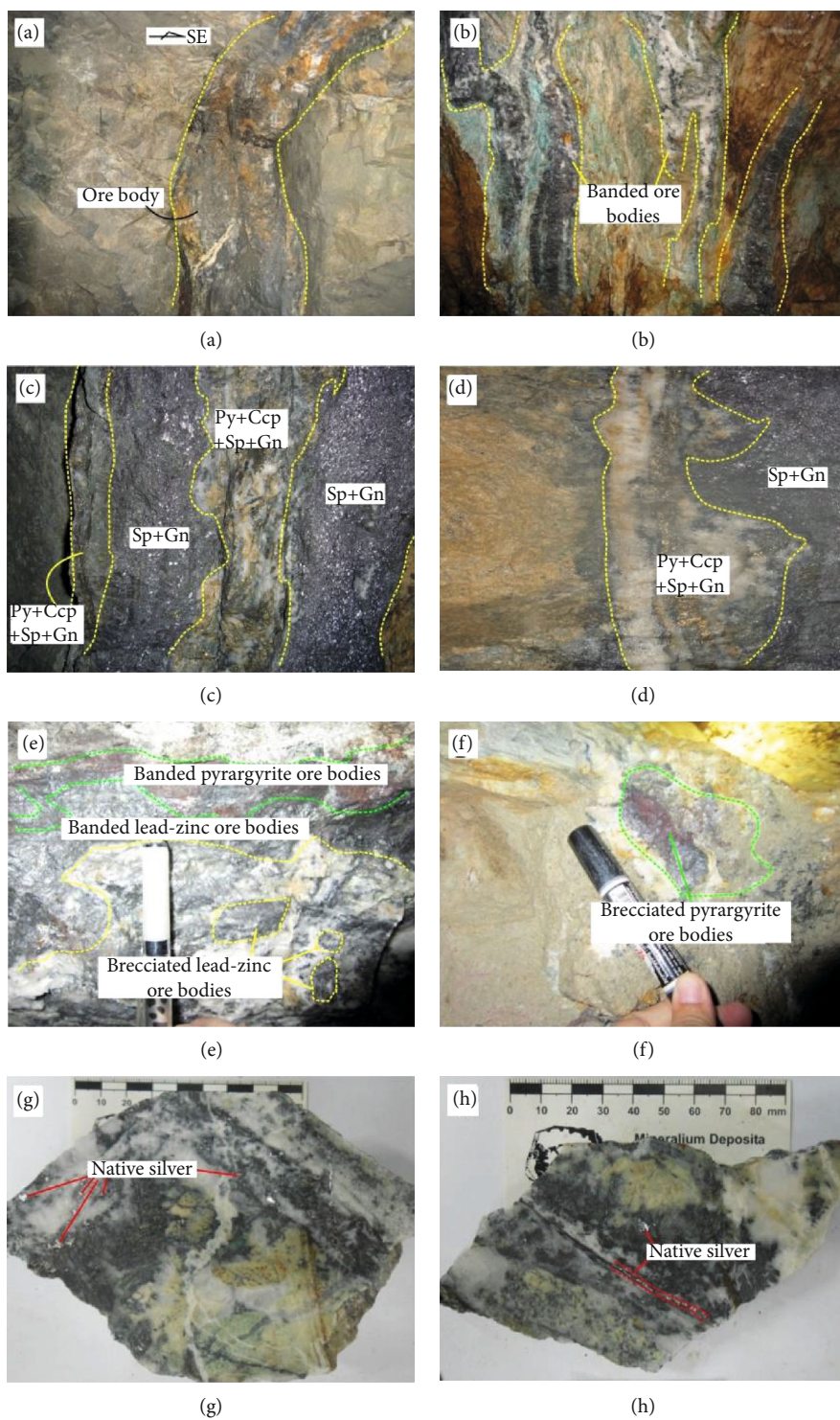


FIGURE 4: Continued.

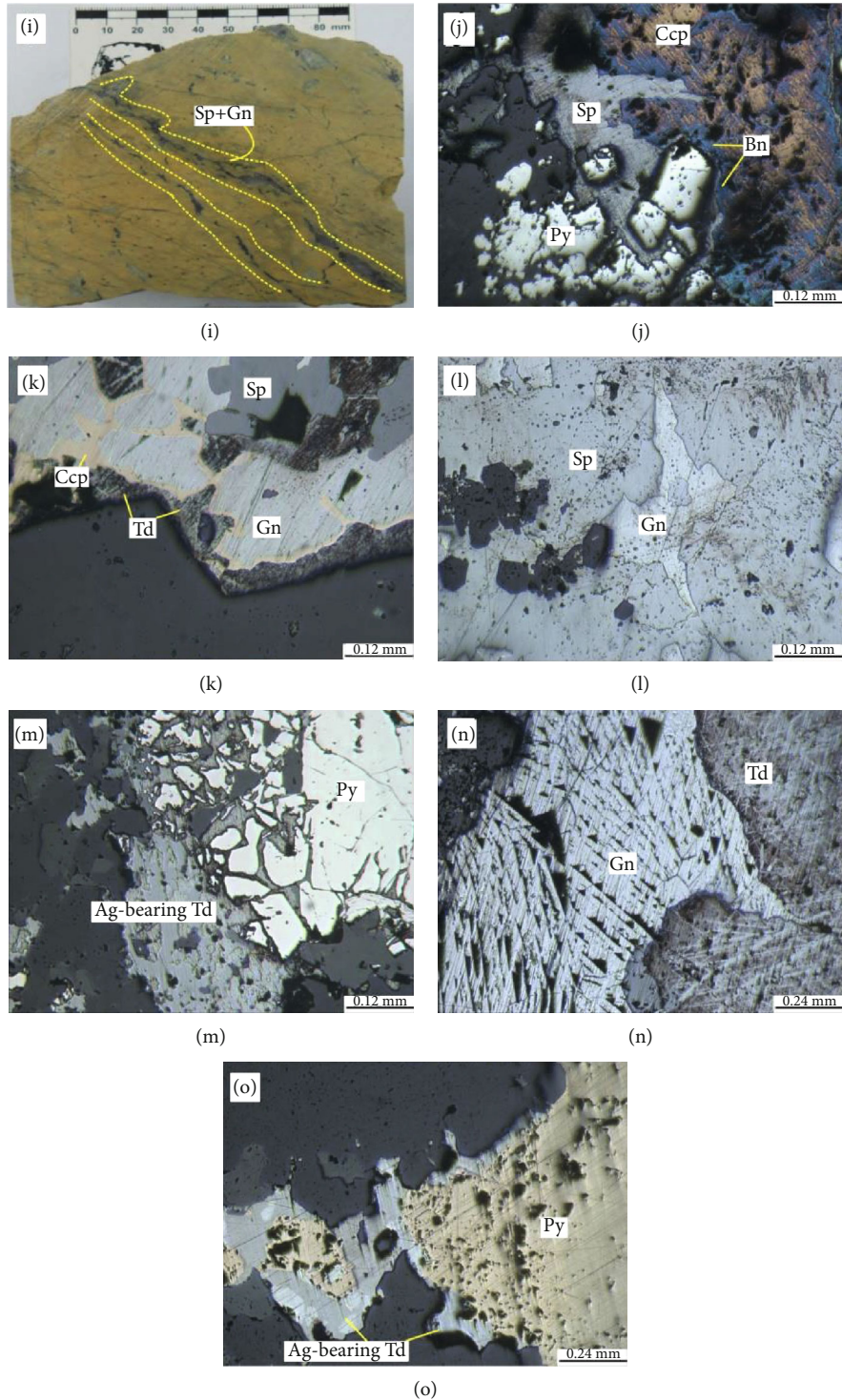


FIGURE 4: Photographs and photomicrographs of the Longmendian ore: (a) Ag–Pb–Zn ore veins; (b) banded Ag–Pb–Zn ore veins; (c) banded Cu–Ag–Pb–Zn ore veins; (d) early native Ag–Gn–Sp vein crosscut by late Py–Ccp–Gn–Sp vein; (e) banded/brecciated Ag–Pb–Zn ores and banded pyrrargyrite ores; (f) brecciated pyrrargyrite ore veins; (g) disseminated native silver in Ag–Pb–Zn veins; (h) veined and disseminated native silver in Ag–Pb–Zn veins; (i) veined Ag–Pb–Zn ores in tuff; (j) Sp (replacing Py) is replaced by Ccp; (k) Td replaced Gn; (l) Gn replaced Sp; (m) Ag-bearing Td replaced Py; (n) Gn replaced Td; (o) Ag-bearing Td replaced Py. Py: pyrite; Gn: galena; Sp: sphalerite; Ccp: chalcopyrite; Td: tetrahedrite.

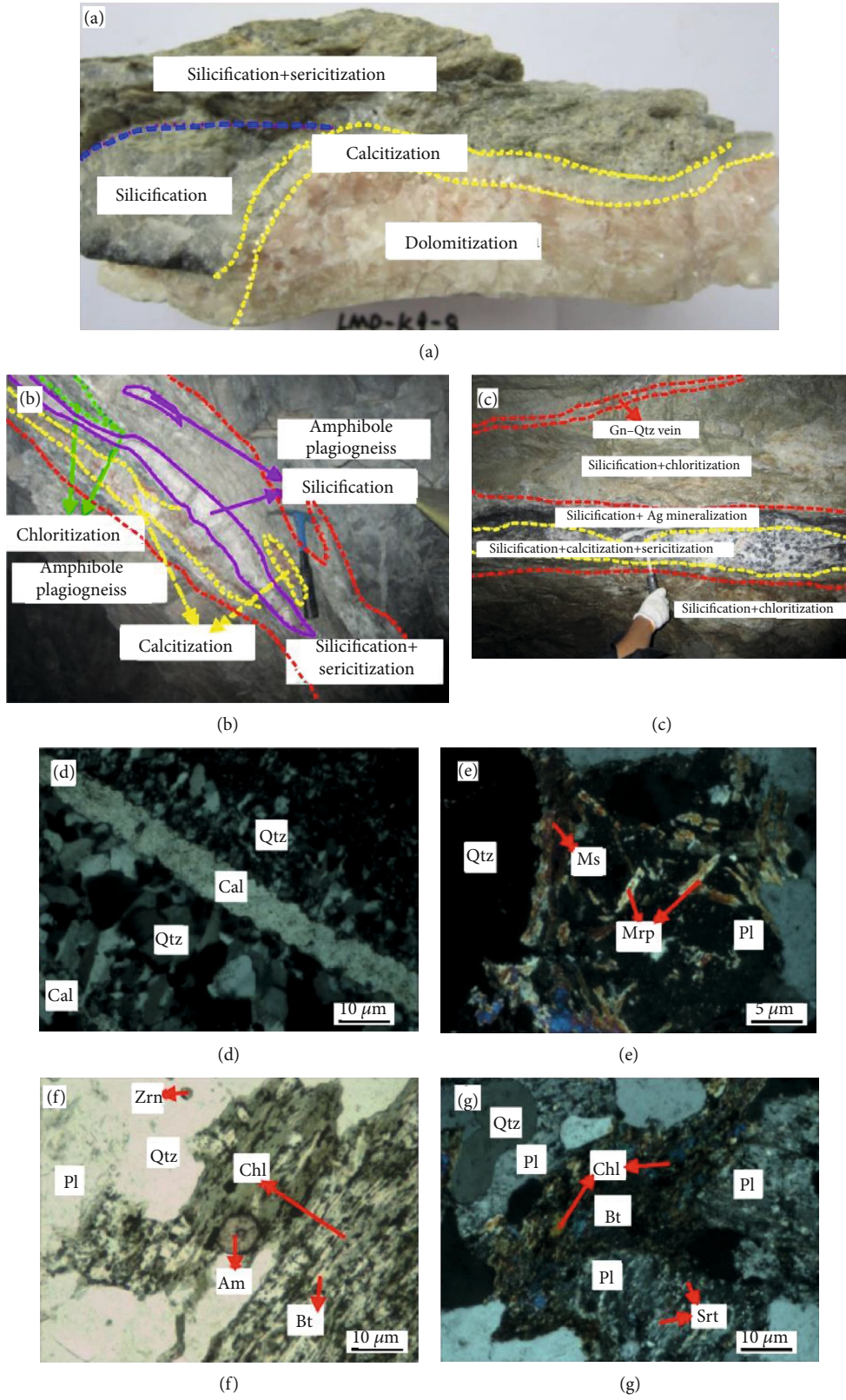


FIGURE 5: Continued.

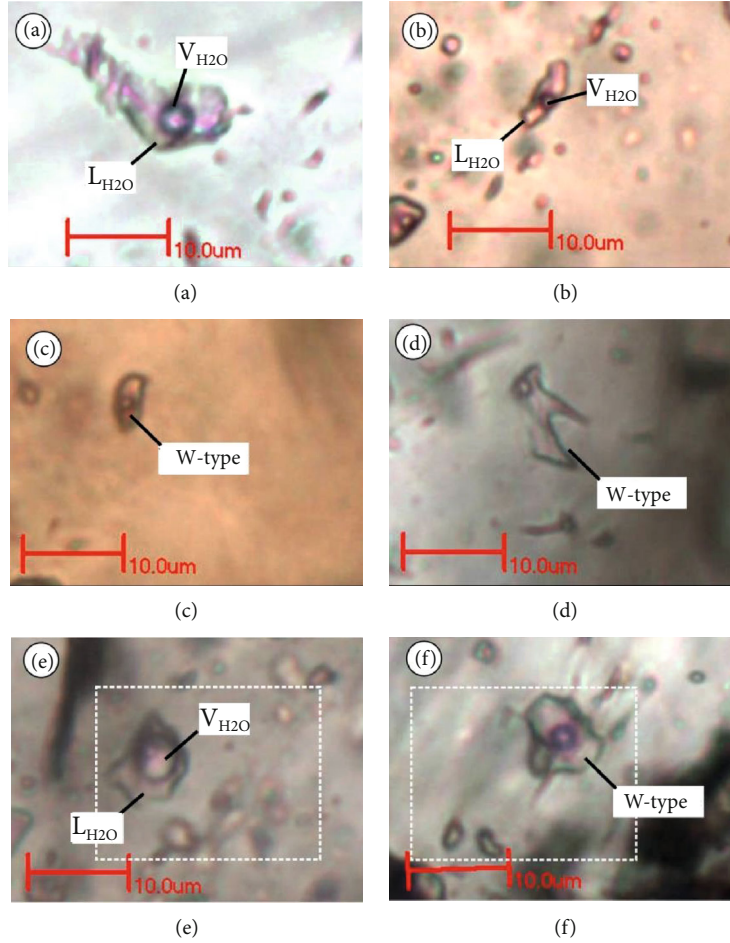


FIGURE 7: Photomicrographs of FI types from Longmudian deposit: (a–d) W-type FIs composed of vapor H_2O and liquid H_2O ; (e–f) different gas-liquid ratios of W-type FIs coexist.

TABLE 1: Microthermometric data of W-type FIs from quartz in the Longmudian Ag-Pb-Zn deposit.

Stage	Minerals	FI type	Tmice (°C)	Thtot (°C)	Salinity (wt% NaCl _{eqv})
1	Quartz	W	-9.4 to -2.4	198 to 332 (L)	4.0 to 13.3
2	Quartz	W	-9.2 to -0.6	132 to 260 (L,V)	1.1 to 4.3 6.6 to 13.1
3	Quartz	W	-4.8 to -1.1	97 to 166 (L)	1.9 to 7.6

Tmice: final melting temperature; Thtot: total homogenization temperature. L and V mean that the FIs homogenized to liquid (L) or vapor (V).

shape. W-type FIs homogenized to liquid or vapor phase by heating.

5.1.2. Thermometry. A total of 152 FIs (from 31 samples) were measured. The thermometric results are given in Table 1 and Figure 8. The homogenization temperatures of Stages 1, 2, and 3 range 198–332°C, 132–260°C, and 97–166°C, respectively. Relations between the freezing

point depression and salinity for the W-type FIs can be expressed as Equation (1) [26]:

$$W = 0.00 + 1.78T_m - 0.042T_m^2 + 0.000557T_m^3, \quad (1)$$

where W is the weight percentage of NaCl (0–23.3 wt% NaCl) and T_m is the freezing point depression (°C). From the measurement, fluid salinity of Stages 1, 2, and 3 are 4.0–13.3, 1.1–13.1, and 1.9–7.6 wt% NaCl_{eqv}, respectively.

5.1.3. Vapor and Liquid Compositions. The vapor and liquid compositions of the FI are listed in Table 2. The vapor phase comprises primarily H_2O and minor CO_2 , H_2 , CO , N_2 , and CH_4 . The liquid phase contains Ca^{2+} , Na^+ , K^+ , SO_4^{2-} , Cl^- , and F^- . For the cations, the Ca^{2+} content is the highest (followed by Na^+), whereas the Mg^+ and K^+ contents are the lowest. For the anions, SO_4^{2-} content is the highest (followed by Cl^-), and the F^- content is the lowest. The ore fluid belongs to a Cl-(SO_4^{2-})-Na-K-(Mg) system.

5.2. H-O Isotope Compositions. For Stage 1, $\delta^{18}O$ values of quartz range from 14.1 to 15.9‰, while $\delta^{18}O_{H_2O}$ values of the fluid in equilibrium with quartz are of 5.8–7.6‰. δD values range from -92 to -76‰. For Stage 2, the

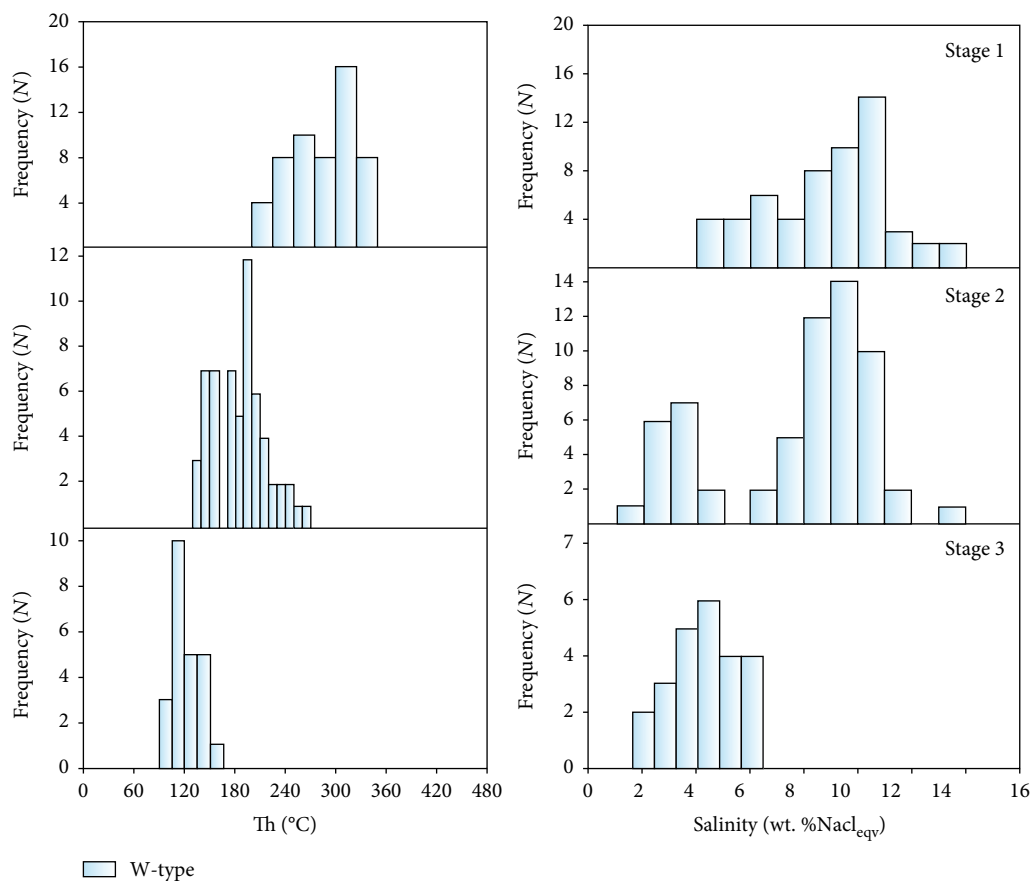


FIGURE 8: Histograms of FI homogenization temperatures and salinities from the Longmendian deposit.

TABLE 2: Vapor and liquid compositions of fluid inclusions ($W_B/10^{-6}$) from the Longmendian deposit.

Sample no. Mineral	Stage 1		Stage 2		Stage 3		
	SJ4-04 Quartz	SJ4-05 Quartz	SJ4-07 Quartz	SJ4-14 Quartz	LMD-06 Calcite	LMD-26 Calcite	
Vapor/ 10^{-6}	H ₂	0.2946	0.2017	0.0617	0.2445	0.7086	0.474
	N ₂	0.0856	0.3077	0.2378	1.239	0.0204	0.2389
	CO	0.0839	0.1116	0.0344	0.0958	14.89	0.158
	CH ₄	0.0871	0.0556	0.0213	0.0804	/	0.0496
	CO ₂	5.043	2.729	4.203	6.032	108.6	14.23
	H ₂ O	98400	117600	224700	274400	113500	85970
Liquid/ 10^{-6}	F ⁻	3.77	1.588	0.1248	0.282	0.5445	1.365
	Cl ⁻	11.37	26.23	43.17	28.33	12.64	3.313
	NO ₃ ⁻	/	0.3314	/	/	/	0.1979
	SO ₄ ²⁻	59.9	100.8	273.9	103.6	16.44	22.71
	Na ⁺	7.502	23.7	28.26	14.97	10.13	5.313
	K ⁺	1.567	2.991	4.386	3.114	2.416	2.04
	Mg ²⁺	1.284	1.436	0.8686	0.5547	18.21	10
	Ca ²⁺	31.96	13.3	49.76	46.11	6.563	21.25

quartz $\delta^{18}\text{O}$, $\delta^{18}\text{O}_{\text{H}_2\text{O}}$, and δD values are of 7.4–11.2‰, –4.4 to –0.6‰, and –81 to –63‰, respectively. For Stage 3, the quartz $\delta^{18}\text{O}$, $\delta^{18}\text{O}_{\text{H}_2\text{O}}$, and δD values are of 6.8–7.9‰, –8.2 to –7.9‰, and –79 to –71‰, respectively (Table 3).

5.3. C-O Isotope Compositions. The C-O isotopic analyses were conducted on 26 calcite samples from Stage 1 to Stage 3 (Table 4). The calcite $\delta^{13}\text{C}_{\text{VPDB}}$ and $\delta^{18}\text{O}_{\text{SMOW}}$ values range from –11.2 to 0.9‰ (avg. –1.67‰) and from 9.21 to 20.86‰ (avg. 13.66‰), respectively.

TABLE 3: H-O isotope data of quartz and calcite from the Longmendian Ag-Pb-Zn deposit (data from this study).

Sample no.	Mineral	Stage	δD	$\delta^{18}O_{V-SMOW}$	$\delta^{18}O_{H_2O}$
ZK1002			-83	15.9	7.6
ZK1002	Quartz	1	-92	14.8	6.5
ZK301			-76	14.1	5.8
ZK702			-89	15.1	6.8
ZK901			-63	9.7	-3.0
ZK1014	Quartz	2	-81	8.3	-4.4
ZK1014			-69	7.4	-5.3
ZK2701			-76	11.2	-1.5
ZK1002	Quartz	3	-79	7.9	-8.9
ZK1002			-71	7.1	-9.7
ZK301	Calcite		-73	6.8	-10.0

TABLE 4: C-O isotope data of calcite from the Longmendian Ag-Pb-Zn deposit.

Sample no.	$\delta^{13}C_{VPDB}$ (‰)	$\delta^{18}O_{SMOW}$ (‰)
LMD-02	0.8	9.21
LMD-04	-2	14.68
LMD-05	0	19.52
LMD-06	-0.1	18.49
LMD-08	0	18.59
LMD-09	-0.1	10.14
LMD-11	-0.1	14.37
LMD-13	-1.1	17.77
LMD-18	0.8	11.177
LMD-20	-0.3	10.04
LMD-21	0.9	11.27
LMD-23	-1.3	14.16
LMD-24	0.9	9.32
LMD-25	-0.2	14.06
LMD-26	0.1	10.45
LMD-29	-6.8	14.57
LMD-30	-0.4	12.2
LMD-32	-7.1	14.57
LMD-47	-4.5	12.41
LMD-48	-2.3	14.57
LMD-49	-1.5	12.82
LMD-51	-1.5	12.61
K8-3	0	11.17
PD1058 K1-1	-1.6	11.58
ZK306-Y1	-4.7	14.47
K23-3	-11.2	20.86

5.4. *S-Pb Isotope Compositions.* The S and Pb isotope data from the Longmendian deposit are listed in Tables 5 and 6, respectively. The pyrite $\delta^{34}S$ values range from -1.42 to 2.35% (avg. 0.26%). The chalcopyrite and galena samples

TABLE 5: Sulfur isotope compositions of pyrite from the Longmendian Ag-Pb-Zn deposit.

Sample no.	$\delta^{34}S_{CDT}$ (‰)
SJ4-03	-1.35
SJ4-03	-1.42
SJ4-04	-0.99
SJ4-05	-0.21
SJ4-06	-0.47
SJ4-09	-0.74
SJ4-09	-0.82
SJ4-11	-0.39
SJ4-11	-0.52
SJ4-12	-0.44
SJ4-14	-0.31
SJ4-21	-0.47
SJ4-22	-0.38
Sj5-1	-0.96
Sj5-2	0.36
Sj5-2	0.57
Sj5-3	0.48
Sj5-5	1.03
SJ2-1	-0.3
SJ41-3	2.35
SJ07-3	1.94
SJ07-3	2
SJ07-4	2.02
SJ07-6	1.49
SJ07-7	1.96
SJ07-10	2.21

have $^{208}Pb/^{204}Pb = 37.771$ to 38.795 , $^{207}Pb/^{204}Pb = 15.388$ to 15.686 , and $^{206}Pb/^{204}Pb = 17.660$ to 18.101 .

6. Discussion

6.1. *Sources of Ore-Forming Material.* The $\delta^{18}O_{H_2O}$ values of Stage 1 ore fluids (5.8 – 7.6% , avg. 6.7%) fall inside the range of magmatic water (5.5 – 9.5%) defined by Sheppard [27], but different from those of the Taihua Group and pegmatite ($\delta^{18}O_{H_2O} = 5.8$ – 6.8% ; [28]). As shown in the $\delta^{18}O_{H_2O}$ vs. δD plot (Figure 9), all Stage 1 data points fall inside/close to the magmatic water field, suggesting a magmatic fluid origin. The Stage 2 $\delta^{18}O_{Qtz}$ (7.4 – 11.2%) and $\delta^{18}O_{H_2O}$ (-4.4 to -0.6% , avg. -2.7%) are lower than their Stage 1 counterparts, and the data points fall between the magmatic water and meteoric water fields (Figure 9), indicating probable meteoric water incursion. Stage 3 data points fall close to the meteoric water line, suggesting that the hydrothermal fluid was dominantly meteoric.

Most data points from the Longmendian, Shagou, Tieluping, and Haopingou deposits fall within the magmatic water field (Figure 10), pointing to a magmatic fluid source. Furthermore, the Longmendian data points also show well-defined linear trend toward the marine carbonate field (Figure 10),

TABLE 6: Lead isotope compositions of sulfides from the Longmendian Ag-Pb-Zn deposit.

Sample no.	Minerals	$^{206}\text{Pb}/^{204}\text{Pb}$	$^{207}\text{Pb}/^{204}\text{Pb}$	$^{208}\text{Pb}/^{204}\text{Pb}$	$t(\text{Ma})$
LMD-DB-5	Chalcopyrite	18.101	15.558	38.478	340
LMD-Nag	Galena	17.88	15.537	38.275	474
LMD-01	Galena	17.954	15.651	38.675	553
LMD-02	Galena	18.018	15.686	38.795	548
LMD-05	Galena	17.931	15.54	38.314	441
LMD-08	Galena	17.89	15.483	38.149	403
LMD-09	Galena	17.881	15.511	38.214	443
LMD-11	Galena	17.952	15.555	38.378	444
LMD-18	Galena	17.825	15.448	38.013	408
LMD-19	Galena	17.828	15.478	38.087	442
LMD-22	Galena	17.833	15.469	38.121	427
LMD-23	Galena	17.66	15.388	37.771	457
LMD-24	Galena	17.856	15.495	38.164	442
LMD-25	Galena	17.784	15.418	37.962	402
LMD-26	Galena	17.694	15.47	38.035	530
LMD-30	Galena	17.834	15.524	38.224	492
LMD-45	Galena	17.879	15.566	38.38	509
LMD-47	Galena	17.758	15.463	38.043	475
LMD-48	Galena	17.76	15.447	38.05	454
LMD-49	Galena	17.739	15.529	38.208	566
LMD-51	Galena	17.764	15.458	38.052	465
LMD-52	Galena	17.784	15.485	38.14	482
LMD-53	Galena	17.828	15.502	38.174	470
LMD-54	Galena	17.791	15.51	38.17	506

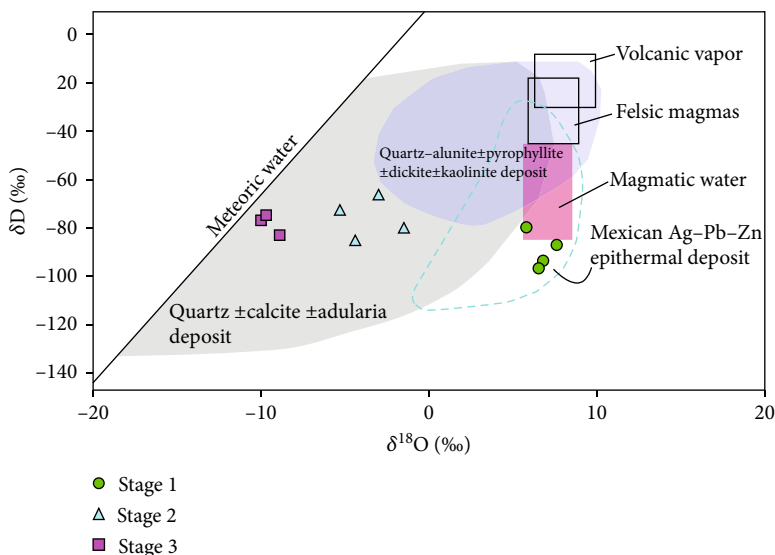


FIGURE 9: δD and calculated $\delta^{18}\text{O}$ values for ore fluids of the Longmendian and other epithermal deposits (modified from [29–32]).

suggesting a marine carbonate input for the ore fluids. Carbonate rocks are abundant in the Longtangou Formation (Taihua Group) and may represent a potential fluid source for the Ag-Pb-Zn mineralization.

The $\delta^{34}\text{S}$ values of hydrothermal minerals depend not only on the source $\delta^{34}\text{S}$ values but also on the physicochemical conditions of the S-bearing fluid migration and precipitation. Ohmoto [35] proposed that the hydrothermal mineral

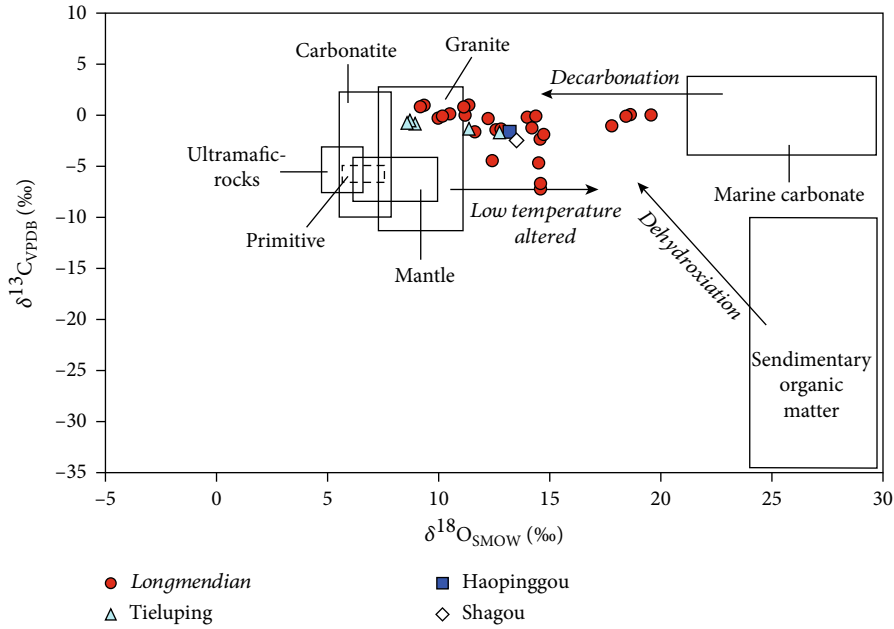


FIGURE 10: $\delta^{13}\text{C}$ and $\delta^{18}\text{O}$ values for ore fluids of the Longmendian and other deposits (modified from [33, 34]).

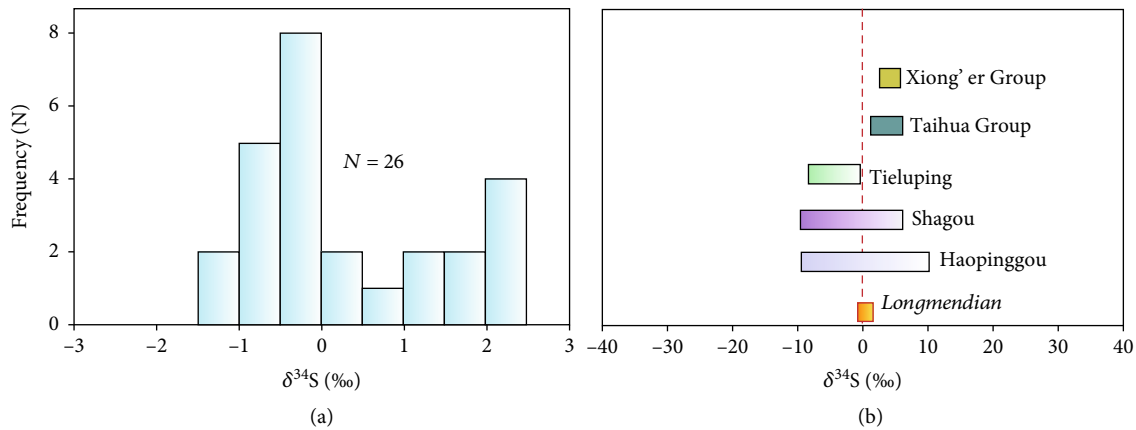


FIGURE 11: Sulfide S isotope compositions from Longmendian and other Ag-Pb-Zn deposits. Data source: the Tieluping, Shagou, and Haopinggou deposits [34]; the Xiong'er Group and Taihua Group [24].

$\delta^{34}\text{S}$ value is a function of the hydrothermal fluid $\delta^{34}\text{S}$ value ($\delta^{34}\text{S}_{\Sigma\text{S}}$), oxygen fugacity (f_{O_2}), temperature (T), pH, and ionic strength (I), i.e., $\delta^{34}\text{S}_{\text{mineral}} = f(\delta^{34}\text{S}_{\Sigma\text{S}}, f_{\text{O}_2}, T, \text{pH}, I)$. He further hypothesized that the fluid $\delta^{34}\text{S}$ value is characterized by a relatively simple mineral assemblage and (with the absence of sulfates) should be similar to that of total sulfide (i.e., $\delta^{34}\text{S}_{\Sigma\text{S}} \approx \delta^{34}\text{S}_{\text{sulfide}}$). No sulfate minerals were found in the Longmendian deposit, and the mineral composition was relatively simple. Therefore, the sulfide $\delta^{34}\text{S}$ could approximate the $\delta^{34}\text{S}_{\Sigma\text{S}}$ of the hydrothermal system. The $\delta^{34}\text{S}$ values of the Longmendian deposit (-1.42 to 2.35‰) are similar to those from magmatic-hydrothermal systems ($0 \pm 5\text{‰}$; [36]) and marginally overlap with the Taihua Gp. metamorphic rocks (Figure 11). This indicates that the sulfur

was likely derived from magmatic-hydrothermal fluids and Taihua Gp. metamorphic rocks.

Polymetallic sulfide (pyrite, chalcopyrite, and galena) from the Longmendian deposit yields a single-stage model age of 340–566 Ma (Table 6), which is inconsistent with the Neoproterozoic Taihua Group metamorphosed terrane (>2.2 Ga) and the regional Ag-Pb-Zn vein-type mineralization (145–133 Ma; see Section 6.3), indicating the presence of excess radiogenic Pb in the fluid system, due to either the decay of U and Th or fluid mixing [37–39]. In a $^{207}\text{Pb}/^{204}\text{Pb}$ vs. $^{206}\text{Pb}/^{204}\text{Pb}$ diagram (Figure 12), the samples plot display a linear correlation. Assuming that the linear distribution of Pb values represents a second isochron (i.e., metallogenesis occurred in multiple phases), we obtain a two-stage model age of 4207–4209 Ma,

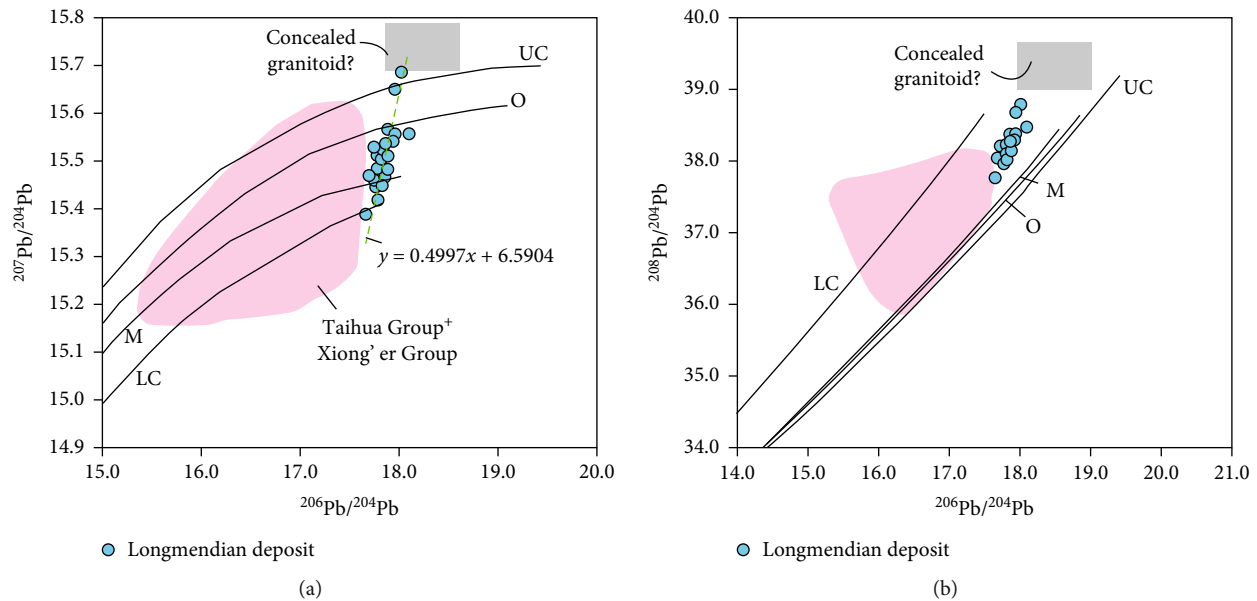


FIGURE 12: Sulfide Pb isotope compositions of the Longmendian deposit. Compositional fields for the upper crust (UC), orogens (O), mantle (M), and lower crust (LC) are from Zartman and Doe [41].

which does not have geological significance (e.g., >3.8 Ma), indicating that the linear relationship records mixing rather than a second isochron. Therefore, we speculate that the ore-forming fluid system at Longmendian was an open system, containing a mixture of external Pb. For a two Pb-source end member mixing system, Pb isotopic data should fall on a line between the two end members [40]. Figure 12 indicates a clear linear relationship for the ore Pb data. Therefore, the ore Pb was likely derived from two end members, one with low radiogenic Pb and the other with high radiogenic Pb contents [40]. On $^{207}\text{Pb}/^{204}\text{Pb}$ vs. $^{206}\text{Pb}/^{204}\text{Pb}$ and $^{208}\text{Pb}/^{204}\text{Pb}$ vs. $^{206}\text{Pb}/^{204}\text{Pb}$ diagrams (Figure 12), the samples plot close to the composition of the metamorphic strata of the Taihua Group and Xiong'er Group, indicating that Pb in the Longmendian deposit was likely derived from the metamorphic strata of the Taihua Group and Xiong'er Group during fluid-rock reaction [38, 39]. In addition, fluids with more radiogenic Pb were probably derived from concealed granitoids.

The ore-forming material of Longmendian deposit mainly derives from magma, and the evidence is as follows: (1) the H–O–C–S–Pb isotope shows that the ore-forming fluid originates from magma. Furthermore, this $\text{Na}^+ - \text{Ca}^{2+} - (\text{K}^+) - \text{SO}_4^{2-} - \text{Cl}^-$ dominated fluids derived from magmatic system also reported in the Jiawula Ag–Pb–Zn deposit [42]. (2) No granite outcrop was found in Longmendian area; only the basic dyke of Paleozoic was found (Figure 3), but the geophysical data also showed that there were concealed intrusions in this area [33]. (3) The wallrock, ore-controlling structure, orebody characteristics, ore minerals, and gangue mineral of the Longmendian deposit were similar to those of the spatially adjacent Haopinggou deposit (Table 7), in which the ore-forming fluid originates from magma [33].

6.2. Ore Fluid Evolution and Ore Precipitation Mechanism

6.2.1. Nature and Evolution of Ore-Forming Fluids. In this study, the ore fluids are determined to be of medium-low temperature and belong to a medium-low salinity $\text{H}_2\text{O} - \text{NaCl}$ system that contains $\text{Na}^+ - \text{Ca}^{2+} - \text{SO}_4^{2-} - \text{Cl}^-$. From Stage 1 to Stage 3, significant changes occur in the FI types and the ore fluid temperature and salinity (Figures 8 and 13), as described in detail as follows:

(1) *Stage 1.* Magmatic intrusion and its subsequent fractionation may have released magmatic fluid to form high-temperature (198–332°C) Stage 1 ore fluids. The salinity-homogenization temperature plot (Figure 13) indicates that the salinity of Stage 1 fluids did not change significantly (4.0–13.3 wt% NaCl_{eqv}), and the major temperature drop could have attributed to cooling.

(2) *Stage 2.* The main-stage mineralization may have contributed by the gradual mixing of magmatic water and meteoric water. The ore fluid temperature and salinity are 132–260°C and 1.1–13.1 wt% NaCl_{eqv} , respectively. The salinity-homogenization temperature plot (Figure 13) shows bimodal fluid salinity, i.e., high salinity (>6 wt% NaCl_{eqv}) and low salinity (<5 wt% NaCl_{eqv}). The coexistence of several FI types (with similar homogenization temperature) further suggests that fluid boiling had taken place (Figures 7(e) and 7(f)).

(3) *Stage 3.* Fluid inclusions in this stage are dominated by W-type. The further temperature and salinity drop (cf. Stage 1 and 2 FIs) in Stage 3 which could be attributed to the continuous incursion of low-temperature and low-salinity meteoric water (Figures 9 and 13).

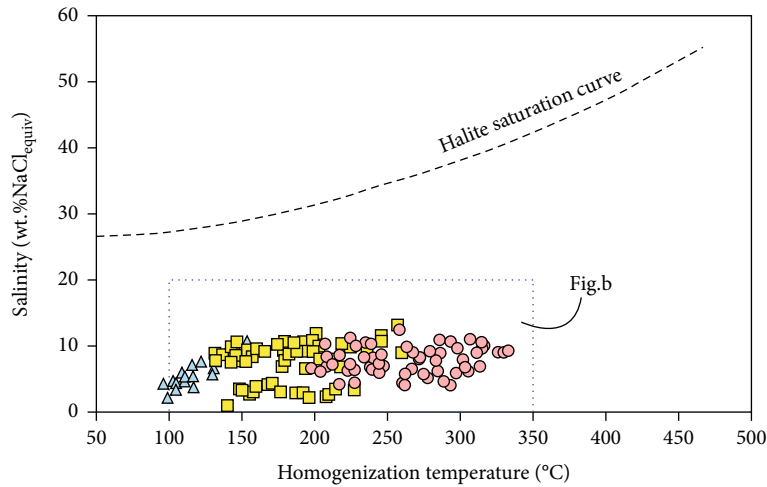
6.2.2. Ore Precipitation Mechanism. In general, silver occurs dominantly as Ag^+ in hydrothermal fluids [43], and is mainly

TABLE 7: Summary of the major features of representative Ag-Pb-Zn deposits in the Xiong'er, eastern Qinling-Dabie Orogen.

Deposit	Host rock	Ore type	Ore mineral	Gangue mineral	Alteration zone	Ore fluid feature	Deposit type	Data source
Longmendian	Taihua Gp. gneiss	Quartz-vein and altered-rock type Au ore	Galena, sphalerite, pyrite, chalcopyrite, silver-bearing tetrahedrite, pyrargyrite, argentite, bornite, native silver, tetrahedrite, polybasite	Quartz, calcite, siderite, ankerite, sericite, fuchsite, muscovite	Silicic; quartz-carbonate-sericite; chlorite-sericite	Medium-low temperature, low salinity CO ₂ -H ₂ O-NaCl system; vapor comprises H ₂ O and CO ₂ , with some H ₂ , CO, N ₂ , and CH ₄ . Liquid phase comprises Ca ²⁺ , Na ⁺ , K ⁺ , SO ₄ ²⁻ , Cl ⁻ , and F ⁻		
Shagou	Taihua Gp. gneiss	Massive and vein-type Ag-bearing lead-zinc ore			Silicic; sericite; chlorite; carbonate	Medium-low temperature, low salinity CO ₂ -H ₂ O-NaCl system	Epithermal	[33]
Tieluping	Taihua Gp. gneiss	Quartz vein type and altered rock type silver ore	Galena, sphalerite, pyrite, chalcopyrite, arsenopyrite, pyrargyrite, silver-bearing tetrahedrite, argentite, bornite, native silver, tetrahedrite, skinnerite, minetisite, domingite	Quartz, sericite, chlorite, plagioclase, potash feldspar, amphibole, biotite, siderite, calcite, ankerite, fuchsite	Silicic; sericite; chlorite; carbonate	Medium-low temperature, low salinity CO ₂ -H ₂ O-NaCl system; vapor comprises H ₂ O, CO ₂ , N ₂ , O ₂ , CO, CH ₄ , C ₂ H ₂ , C ₂ H ₄ , and C ₂ H ₆	Epithermal	[34]
Haopinggou	Taihua Gp. gneiss	Quartz vein type and altered rock type silver ore			Silicic; sericite; chlorite; carbonate	Medium-low temperature, low salinity H ₂ O-NaCl system	Epithermal	[33]

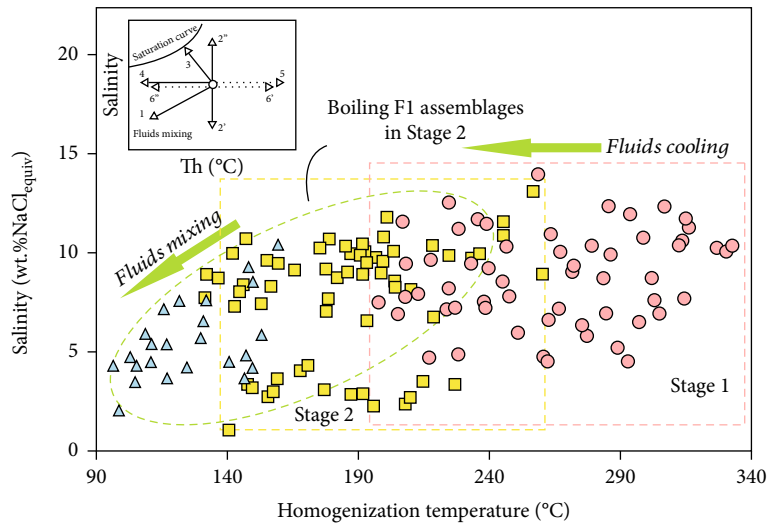
transported as silver chloride (AgCl²⁻) or/and silver bisulfide complexes (AgHS⁰) in the fluids [44, 45]. Under lower temperatures (<200°C), AgHS⁰ complexes occur dominantly under near-neutral conditions, whereas AgCl²⁻ complexes occur largely under (mildly)-acidic conditions (e.g., [46, 47]). Under higher temperatures (>400°C), silver is transported dominantly in AgCl²⁻ complexes, whereas AgHS⁰ species are only stable under (mildly)-alkaline conditions (e.g., [44, 48]). The Longmendian ore fluids were in equilibrium with montmorillonite-sericite-quartz and K-feldspar-muscovite-quartz assemblages, which yielded pH = 4.5–6.5 at 200–350°C [49, 50]. The Stage 1 and 2 fluids are featured by medium to low temperatures (avg. 291°C and 185°C, respectively), and thus, the silver may have transported mainly in AgHS⁰ complexes (e.g., [46, 47, 51]). In these fluids, Zn can be transported in both Zn-Cl and Zn(HS)₃⁻ complexes [52, 53]. Lead chloride complexes are usually important for Pb transport in intermediate-to-high-salinity fluids [54]. Our FI compositional analysis also shows that Cl⁻ and SO₄²⁻ contents are high in the Longmendian ore fluid (Table 2).

Generally, vein-type ore precipitation in hydrothermal deposits can be triggered by fluid boiling, mixing, and/or simply cooling [55–58]. The physicochemical changes on the fluids by boiling would affect Ag sulfide saturation via H₂S degassing and/or pH increase [48]. pH increases quite drastically during boiling, especially in Stage 2 because of degassing of CO₂ and to a lesser extent H₂S. Conductive cooling leads to pH decrease, plus minor effect on aqueous species activities [48]. The fluid cooling and pH increase caused by mixing with meteoric water (seawater or other high-pH fluids) may have led to Zn deposition because of (i) change in the dominating Zn complex (Zn-Cl complexes in high-temperature acidic fluids and Zn(HS)₃⁻ and ZnS(HS) in low-temperature and alkaline fluids), and (ii) Zn solubility drop because of pH increase. Previous experimental studies have shown that temperature drop can effectively dissociate zinc- and lead-chloride complexes (e.g., [59]). As discussed above, fluid inclusion and H-C-O isotope evidence points to fluid boiling, mixing, and cooling at Stage 2 (Figures 8 and 13), which likely formed the quartz-polymetallic sulfide ore veins.



Stage 1: ● W-type
 Stage 2: ■ W-type
 Stage 3: ▲ W-type

(a)



Stage 1: ● W-type
 Stage 2: ■ W-type
 Stage 3: ▲ W-type

(b)

FIGURE 13: Th vs. salinity of fluid inclusions in the Longmendian deposit (a). Possible fluid evolution trends shown in the temperature–salinity plot (b).

6.3. *Metallogenetic Mechanism.* Previous studies have reported the K-Ar/Ar–Ar ages and molybdenite Re-Os model ages of the Ag-Pb-Zn-Mo deposits in the study area [3–11]. The mineralization ages reported fall into two groups: Paleoproterozoic (1888–1686 Ma) and Early Cretaceous (145–133 Ma). The Paleoproterozoic phase has formed the Zhai’ao and the Longmendian Mo deposits. The Early Cretaceous has formed the Tieluping, Shagou, and Haopinggou deposits. Although ca. 1888 Ma molybdenite Re–Os isochron age was obtained [15], the existence of molybdenite in the Pb-Zn-Ag-quartz veins has not been confirmed, and thus, the Paleoproterozoic

age may reflect an earlier mineralization phase before the Ag-Pb-Zn vein-type mineralization.

The ore deposit geology (wallrock, ore-controlling structure) and ore/gangue mineral assemblages of the Longmendian deposit resemble those of the nearby Haopinggou, Shagou, and Tieluping deposits (Table 7), and hence, these broadly coeval (145–133 Ma) deposits may belong to the same Ag-Pb-Zn mineral system. Vein-type Ag-Pb-Zn mineralization at Shagou, Haopinggou, Tieluping, and Longmendian can be attributed to crustal extension-related (Figure 14; [18]) because (1) Late Mesozoic granitoids

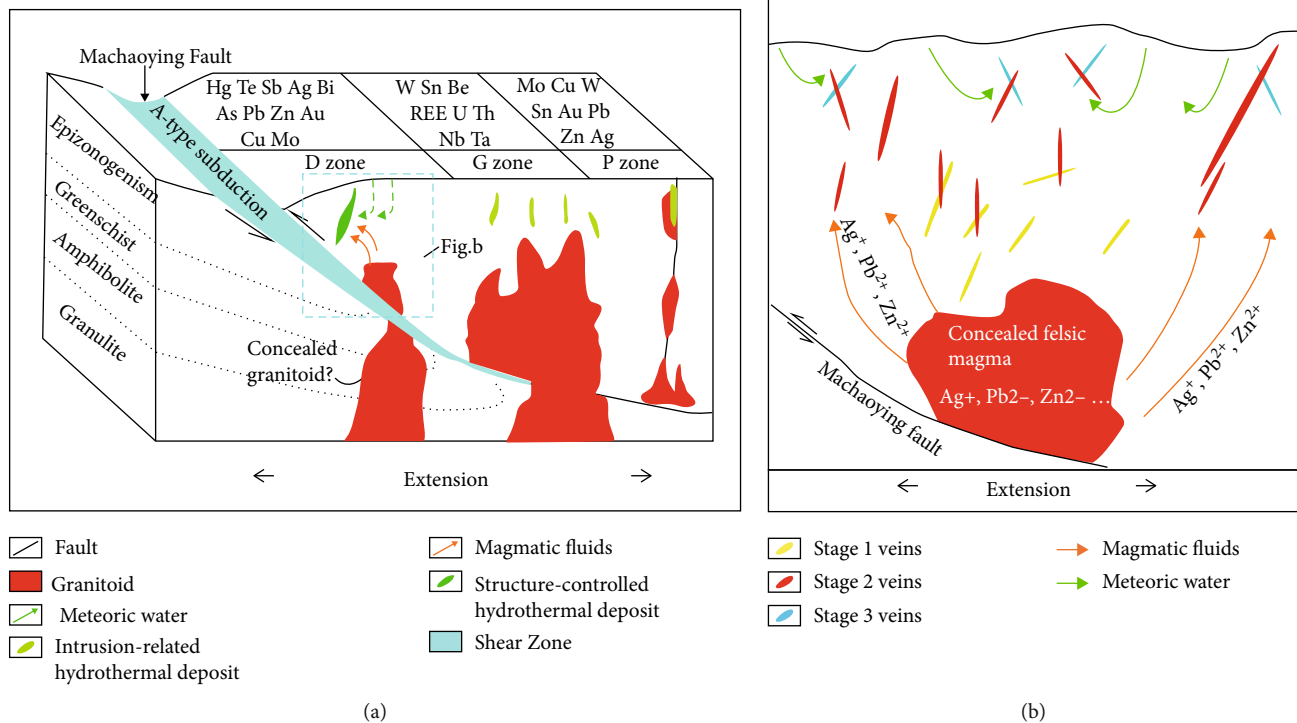


FIGURE 14: Metallogenic model for the Shagou (Xiayu) Ag-Pb-Zn ore field (modified after [67, 68]) (a). The genetic model for Ag-Pb-Zn vein formation at Longmendian deposit (modified after [42, 59]) (b). D: hydrothermal lode deposits; G: granites and their related deposits; P: porphyries, breccia pipes, their related deposits.

(157–127 Ma; [24, 60, 61]) contain abundant mafic microgranular enclaves (MMEs), which are interpreted to represent mixing of mafic and felsic magmas [62, 63]. In addition, some of the MME-bearing plutons are intruded by slightly younger mafic dykes [7, 62–64]. (2) The presence of Early Cretaceous Xiong'er, Xiaoshan, and Xiaoqinling metamorphic core complexes (Figure 1; [65, 66]) demonstrates that large parts of the southern NCC were dominated by extensional tectonics. This extensional event may have linked to lithospheric thinning caused by the west-dipping Paleo-Pacific subduction, which led to partial decratonization of the NCC [7, 8, 24].

The mineralization was strictly controlled by the NE-NNE-trending fault zones. The Ag-Pb-Zn ore-forming temperature (132–260°C) is low to medium, while the ore fluids progressed from dominantly magmatic-sourced to magmatic-meteoric mixed. The S and Pb isotope compositions indicate that the ore-forming materials were primarily originated from the magma with input from the metamorphosed sequences. Geological and geochemical features suggest that the Longmendian deposit likely belongs to medium-to-low temperature hydrothermal-type related to Cretaceous granitic magmatism (Figure 14).

At Longmendian, the ore minerals comprise galena, sphalerite, pyrite, chalcocopyrite, (Ag-bearing)-tetrahedrite, and native silver, resembling typical low-sulfidation to intermediate-sulfidation (LS/IS) epithermal mineralization. The LS/IS epithermal affinity is also reflected in the alteration mineral assemblage (quartz+calcite+adularia+illite), intermediate-low

ore fluid temperature (150–320°C), and bimodal salinity (<5% NaCl_{eqv} and >6% NaCl_{eqv}) that suggests fluid boiling.

7. Conclusions

- (1) The H-C-O isotope evidence indicates that the ore fluids were derived from magmatic water with increasing meteoric water input toward the later ore stages. The S-Pb isotope evidence indicates that the ore-forming materials were mainly originated from the granitic magma and the Taihua Group wallrocks
- (2) Ore-forming fluids were largely of medium-low temperature and medium-low salinity, belonging to a low-density H₂O-NaCl system that contains Na⁺-Ca²⁺-SO₄²⁻-Cl⁻. Fluid boiling and cooling, and mixing with meteoric water, may have contributed to the ore precipitation

Mineralization at Longmendian shares similar geological characteristics (in lithology, structure, ore/gangue assemblage, and ore fluid temperature and salinity) with typical low-sulfidation to intermediate-sulfidation (LS/IS) epithermal deposits.

Data Availability

The data used to support the findings of this study are included within the article.

Conflicts of Interest

The authors declare no conflict of interest.

Authors' Contributions

Xinling Chen, Cheng Wang, and Yongjun Shao conceived and designed the experiment. Cheng Wang and Xinling Chen performed the experiment. All authors wrote the paper.

Acknowledgments

This work was supported by the Innovation-Driven Project of Central South University (2018zzts196) and the Open Topic of Hunan Key Laboratory of Land Resources Evaluation and Utilization (Project SYS-ZX-201804).

References

- [1] J. Mao, R. Goldfarb, Z. Zhang, W. Xu, Y. Qiu, and J. Deng, "Gold deposits in the Xiaoqinling-Xiong'ershan region, Qinling Mountains, Central China," *Mineralium Deposita*, vol. 37, no. 3-4, pp. 306-325, 2002.
- [2] M. G. Zhai, "Tectonic evolution and metallogenesis of North China Craton," *Mineral Deposits*, vol. 29, pp. 24-36, 2010.
- [3] J. W. Mao, F. Pirajno, J. F. Xiang et al., "Mesozoic molybdenum deposits in the east Qinling-Dabie orogenic belt: characteristics and tectonic settings," *Ore Geology Reviews*, vol. 43, no. 1, pp. 264-293, 2011.
- [4] J. W. Mao, G. Q. Xie, F. Bierlein et al., "Tectonic implications from Re-Os dating of Mesozoic molybdenum deposits in the East Qinling-Dabie orogenic belt," *Geochimica et Cosmochimica Acta*, vol. 72, no. 18, pp. 4607-4626, 2008.
- [5] M. Mi, Y.-J. Chen, Y.-F. Yang et al., "Geochronology and geochemistry of the giant Qian'echong Mo deposit, Dabie Shan, eastern China: implications for ore genesis and tectonic setting," *Gondwana Research*, vol. 27, no. 3, pp. 1217-1235, 2015.
- [6] Y. J. Chen, F. Pirajno, and Y. H. Sui, "Isotope geochemistry of the Tieluping silver-lead deposit, Henan, China: a case study of orogenic silver-dominated deposits and related tectonic setting," *Mineralium Deposita*, vol. 39, no. 5-6, pp. 560-575, 2004.
- [7] J.-W. Li, S.-J. Bi, D. Selby et al., "Giant Mesozoic gold provinces related to the destruction of the North China Craton," *Earth and Planetary Science Letters*, vol. 349-350, pp. 26-37, 2012.
- [8] J.-W. Li, Z.-K. Li, M.-F. Zhou et al., "The early Cretaceous Yangzhaiyu lode gold deposit, North China Craton: a link between craton reactivation and gold veining," *Economic Geology*, vol. 107, no. 1, pp. 43-79, 2012.
- [9] N. Li, Y.-J. Chen, F. Pirajno, and Z.-y. Ni, "Timing of the Yuchiling giant porphyry Mo system, and implications for ore genesis," *Mineralium Deposita*, vol. 48, no. 4, pp. 505-524, 2013.
- [10] S. J. Bi, J. W. Li, and Z. K. Li, "Geological significance and geochronology of Paleoproterozoic mafic dykes of Xiaoqinling gold district, southern margin of the North China Craton," *Earth Science-Journal of China University of Geosciences*, vol. 36, pp. 17-32, 2011.
- [11] K.-F. Tang, J.-W. Li, D. Selby, M.-F. Zhou, S.-J. Bi, and X.-D. Deng, "Geology, mineralization, and geochronology of the Qianhe gold deposit, Xiong'ershan area, southern North China Craton," *Mineralium Deposita*, vol. 48, no. 6, pp. 729-747, 2013.
- [12] J. J. Gao, J. W. Mao, M. H. Chen, H. S. Ye, J. J. Zhang, and Y. F. Li, "Vein structure analysis and $^{40}\text{Ar}/^{39}\text{Ar}$ dating of sericite from sub-ore altered rocks in the Tieluping large-size Ag-Pb deposit of Western Henan Province," *Acta Geologica Sinica*, vol. 85, pp. 1172-1187, 2011.
- [13] C. H. Yan and G. Y. Liu, "Metallogenic characteristics and ore-prospecting suggestions of lead-zinc polymetallic deposits in southwestern Henan Province of China," *Geological Bulletin of China*, vol. 23, pp. 1143-1148, 2004.
- [14] H. S. Ye, *The Mesozoic Tectonic Evolution and Pb-Zn-Ag Metallogeny in the South Marlin of North China Craton*, [Ph.D. thesis], Chinese Academy of Geological Sciences, Beijing, China, 2006.
- [15] Q. G. Wei, J. M. Yao, T. P. Zhao et al., "Discovery of a 1.9 Ga Mo deposit in the eastern Qinling orogen: molybdenite Re-Os ages of the Longmenidan Mo deposit in Henan Province," *Acta Petrologica Sinica*, vol. 25, pp. 2747-2751, 2009.
- [16] X. H. Deng, J. M. Yao, J. Li, and Y. L. Sun, "Molybdenite Re-Os isotope age of the Zhaiwa Mo deposit and implications for Xiongerian mineralization in eastern Qinling Orogen," *Acta Petrologica Sinica*, vol. 25, pp. 2739-2746, 2009.
- [17] N. Li, Y. J. Chen, X. H. Deng, and J. M. Yao, "Fluid inclusion geochemistry and ore genesis of the Longmendian Mo deposit in the East Qinling Orogen: implication for migmatitic-hydrothermal Mo-mineralization," *Ore Geology Reviews*, vol. 63, pp. 520-531, 2014.
- [18] Z.-K. Li, J. W. Li, X. F. Zhao et al., "Crustal-extension Ag-Pb-Zn veins in the Xiong'ershan District, Southern North China Craton: constraints from the Shagou deposit," *Economic Geology*, vol. 108, no. 7, pp. 1703-1729, 2013.
- [19] Z.-K. Li, J.-W. Li, D. R. Cooke et al., "Textures, trace elements, and Pb isotopes of sulfides from the Haopinggou vein deposit, southern North China Craton: implications for discrete Au and Ag-Pb-Zn mineralization," *Contributions to Mineralogy and Petrology*, vol. 171, no. 12, 2016.
- [20] Y. J. Shao, X. L. Chen, Y. F. Li, Q. Q. Liu, and J. D. Zhang, "Characteristics of geochemistry and genesis of Longmendian Ag-Pb-Zn deposit, Western Henan Province," *Journal of Central South University (Science and Technology)*, vol. 46, no. 1, pp. 171-179, 2015.
- [21] J. L. Li, *Metallogenic Regularities and Metallogenic Prediction of Gold Deposits in the Eastern Xiong'ershan Section of Henan Province*, [M.S. thesis], Central South University, Changsha, 2010.
- [22] F. G. Ren, H. M. Li, Y. J. Yin, S. B. Li, S. Y. Ding, and Z. H. Chen, "Study of isotopic geochronology of Xionger Group Henan Province, China," *Progress in Precambrian Research*, vol. 25, no. 1, pp. 41-47, 2002.
- [23] N. Li, Y. L. Sun, J. Li, L. W. Xue, and W. B. Li, "Molybdenite Re-Os isotope age of the Dahu Au-Mo deposit, Xiaoqinling and the Indosinian mineralization," *Acta Petrologica Sinica*, vol. 24, no. 4, pp. 810-816, 2008.
- [24] J.-W. Mao, G.-Q. Xie, F. Pirajno et al., "Late Jurassic-early Cretaceous granitoid magmatism in Eastern Qinling, Central-Eastern China: SHRIMP zircon U-Pb ages and tectonic implications," *Australian Journal of Earth Sciences*, vol. 57, no. 1, pp. 51-78, 2010.
- [25] E. Roedder, "Fluid inclusions," *Reviews in Mineralogy*, vol. 12, pp. 25-35, 1984.

- [26] D. L. Hall, S. M. Sterner, and R. J. Bodnar, "Freezing point depression of NaCl-KCl-H₂O solutions," *Economic Geology*, vol. 83, no. 1, pp. 197–202, 1988.
- [27] S. M. F. Sheppard, "Chapter 6. characterization and isotopic variations in natural waters," in *Stable Isotopes in High Temperature Geological Processes*, J. W. Valley, H. P. Taylor, and J. R. O'Neil, Eds., vol. 16 of Reviews in Mineralogy. Mineralogical Society of America, pp. 165–184, De Gruyter, Berlin, Boston, 1986.
- [28] H. R. Fan, Y. H. Xie, R. Zhao, and Y. L. Wang, "Stable isotope geochemistry of rocks and gold deposits in the Xiongershan, Henan province," *Contributions to Geology and Mineral Resources Research*, vol. 9, pp. 54–64, 1994.
- [29] A. Arribas, "Characteristics of high-sulfidation epithermal deposits, and their relation to magmatic fluid," *Mineralogical Association of Canada Short Course*, vol. 23, pp. 419–454, 1995.
- [30] T. Albinson, D. I. Norman, D. Cole, and B. Chomiak, "Controls on formation of low-sulfidation epithermal deposits in Mexico: constraints from fluid inclusion and stable isotope data," *Society of Economic Geologists Special Publication*, vol. 8, pp. 1–32, 2001.
- [31] D. R. Cooke and S. F. Simmons, "Characteristics and genesis of epithermal gold deposits," *Reviews in Economic Geology*, vol. 13, pp. 221–244, 2000.
- [32] S. F. Simmons, "Magmatic contributions to low-sulfidation epithermal deposits: magmas, fluids and ore deposits," *Mineralogical Society of Canada Short Course*, vol. 23, pp. 455–477, 1995.
- [33] J. J. Gao, *Geology and Ore-Forming Fluid of Silver-Lead-Zinc Lode Deposit of Shagou, Western Henan Province*, [M.S. thesis], China University of Geosciences, Beijing, China, 2007.
- [34] W. Chen, S. R. Guo, and B. Chui, "Isotopic geochemistry of the Tieluping and Haopinggou deposits in the mount Xiong'er area western Henan," *Geological Exploration for Non-ferrous Metals*, vol. 5, pp. 213–218, 1996.
- [35] H. Ohmoto, "Systematics of sulfur and carbon isotopes in hydrothermal ore deposits," *Economic Geology*, vol. 67, no. 5, pp. 551–578, 1972.
- [36] M. Chaussidon and J. P. Lorand, "Sulphur isotope composition of orogenic spinel lherzolite massifs from Ariege (North-Eastern Pyrenees, France): an ion microprobe study," *Geochimica et Cosmochimica Acta*, vol. 54, no. 10, pp. 2835–2846, 1990.
- [37] A. Johansson, "Lead isotope composition of Caledonian sulfide-bearing veins in Sweden," *Economic Geology*, vol. 78, no. 8, pp. 1674–1688, 1983.
- [38] J. Horner, F. Neubauer, W. H. Paar, W. Hansmann, V. Koeppel, and K. Robl, "Structure, mineralogy, and Pb isotopic composition of the As–Au–Ag deposit Rotgülden, Eastern Alps (Austria): significance for formation of epigenetic ore deposits within metamorphic domes," *Mineralium Deposita*, vol. 32, no. 6, pp. 555–568, 1997.
- [39] H. Y. Chen, Y. J. Chen, and M. Baker, "Isotopic geochemistry of the Sawayaerdun orogenic-type gold deposit, Tianshan, northwest China: Implications for ore genesis and mineral exploration," *Chemical Geology*, vol. 310–311, pp. 1–11, 2012.
- [40] J. T. Peng, R. Z. Hu, and W. C. Su, "Lead isotopic composition of ores in the antimony deposits at the southern margin of the Yangtze massif and its geological implication," *Geology–Geochemistry*, vol. 28, no. 4, pp. 43–47, 2000.
- [41] R. E. Zartman and B. R. Doe, "Plumbotectonics—the model," *Tectonophysics*, vol. 75, no. 1–2, pp. 135–162, 1981.
- [42] D.-G. Zhai, J.-J. Liu, J.-P. Wang et al., "Fluid evolution of the Jiawula Ag-Pb-Zn deposit, Inner Mongolia: mineralogical, fluid inclusion, and stable isotopic evidence," *International Geology Review*, vol. 55, no. 2, pp. 204–224, 2012.
- [43] A. E. Williams-Jones and A. A. Migdisov, "Experimental constraints on the transport and deposition of metals in ore-forming hydrothermal systems," *Society of Economic Geologists*, vol. 18, pp. 77–96, 2014.
- [44] A. Stefánsson and T. M. Seward, "Experimental determination of the stability and stoichiometry of sulphide complexes of silver(I) in hydrothermal solutions to 400°C," *Geochimica et Cosmochimica Acta*, vol. 67, no. 7, pp. 1395–1413, 2003.
- [45] A. A. Migdisov and A. E. Williams-Jones, "A predictive model for metal transport of silver chloride by aqueous vapor in ore-forming magmatic-hydrothermal systems," *Geochimica et Cosmochimica Acta*, vol. 104, pp. 123–135, 2013.
- [46] T. M. Seward, "The stability of chloride complexes of silver in hydrothermal solutions up to 350°C," *Geochimica et Cosmochimica Acta*, vol. 40, no. 11, pp. 1329–1341, 1976.
- [47] C. H. Gammons and H. L. Barnes, "The solubility of Ag₂S in near-neutral aqueous sulfide solutions at 25 to 300°C," *Geochimica et Cosmochimica Acta*, vol. 53, no. 2, pp. 279–290, 1989.
- [48] C. H. Gammons and A. E. Williams-Jones, "Hydrothermal geochemistry of electrum; thermodynamic constraints," *Economic Geology*, vol. 90, no. 2, pp. 420–432, 1995.
- [49] H. Ohmoto and B. J. Skinner, "The Kuroko and related volcanogenic massive sulfide deposits: introduction and summary of new findings," in *The Kuroko and Related Volcanogenic Massive Sulfide Deposits*, vol. 5 of Economic Geology, pp. 1–8, Society of Economic Geologists, 1983.
- [50] J. M. Franklin, J. W. Lydon, and D. F. Sangster, "Volcanic associated massive sulphide deposits," in *economic geology seventy-fifth anniversary volume*, pp. 485–627, The Economic Geology Publishing Company, 1981.
- [51] D. Zhai, J. Liu, N. J. Cook et al., "Mineralogical, textural, sulfur and lead isotope constraints on the origin of Ag-Pb-Zn mineralization at Bianjiadayuan, Inner Mongolia, NE China," *Mineralium Deposita*, vol. 54, no. 1, pp. 47–66, 2019.
- [52] B. R. Tagirov, O. M. Suleimenov, and T. M. Seward, "Zinc complexation in aqueous sulfide solutions: determination of the stoichiometry and stability of complexes via ZnS_(cr) solubility measurements at 100 °C and 150 bars," *Geochimica et Cosmochimica Acta*, vol. 71, no. 20, pp. 4942–4953, 2007.
- [53] B. R. Tagirov and T. M. Seward, "Hydrosulfide/sulfide complexes of zinc to 250 °C and the thermodynamic properties of sphalerite," *Chemical Geology*, vol. 269, no. 3–4, pp. 301–311, 2010.
- [54] T. M. Seward, "The formation of lead(II) chloride complexes to 300°C: a spectrophotometric study," *Geochimica et Cosmochimica Acta*, vol. 48, no. 1, pp. 121–134, 1984.
- [55] A. Hezarkhani, A. E. Williams-Jones, and C. H. Gammons, "Factors controlling copper solubility and chalcopyrite deposition in the Sungun porphyry copper deposit, Iran," *Mineralium Deposita*, vol. 34, no. 8, pp. 770–783, 1999.
- [56] T. Ulrich, D. Gunther, and C. A. Heinrich, "The evolution of a porphyry Cu–Au deposit, based on LA-ICP-MS analysis of fluid inclusions: Bajo de la Alumbrera, Argentina," *Economic Geology*, vol. 97, no. 8, pp. 1889–1920, 2002.

- [57] S. F. Simmons, N. C. White, and D. John, "Geological characteristics of epithermal precious and base metal deposits," *Economic Geology*, pp. 485–522, 2005.
- [58] A. E. Williams-Jones, I. M. Samson, K. M. Ault, J. E. Gagnon, and B. J. Fryer, "The genesis of distal zinc skarns: evidence from the Mochito Deposit, Honduras," *Economic Geology*, vol. 105, no. 8, pp. 1411–1440, 2010.
- [59] Y. Ma, S.-Y. Jiang, R.-S. Chen, X.-X. Li, L. Zhu, and S.-F. Xiong, "Hydrothermal evolution and ore genesis of the Zhaiping Ag-Pb-Zn deposit in Fujian Province of Southeast China: evidence from stable isotopes (H, O, C, S) and fluid inclusions," *Ore Geology Reviews*, vol. 104, pp. 246–265, 2019.
- [60] J. J. Gao, J. W. Mao, H. S. Ye, M. H. Chen, and R. F. Zheng, "Geology and ore-forming fluid of silver-lead-zinc lode deposit of Shagou, western Henan Province," *Acta Petrologica Sinica*, vol. 26, pp. 740–756, 2010.
- [61] B. Guo, L. M. Zhu, B. Li, H. J. Gong, and J. Q. Wang, "Zircon U-Pb age and Hf isotope composition of the Huashan and Heyu granite plutons at the southern margin of North China craton: implications for geodynamic setting," *Acta Petrologica Sinica*, vol. 25, pp. 265–281, 2009.
- [62] L. X. Ding, C. Q. Ma, J. W. Li, L. X. Wang, L. Chen, and Z. B. She, "LA-ICPMS zircon U-Pb ages of the Lantian and Muhuguan granitoid plutons, southern margin of the North China craton: implications for tectonic setting," *Geochimica*, vol. 39, pp. 401–413, 2010.
- [63] R. Liu, J. W. Li, S. J. Bi, H. Hu, and M. Chen, "Magma mixing revealed from in situ zircon U-Pb-Hf isotope analysis of the Muhuguan granitoid pluton, eastern Qinling orogen, China: implications for late Mesozoic tectonic evolution," *International Journal of Earth Sciences*, vol. 102, no. 6, pp. 1583–1602, 2013.
- [64] Z. W. Bao, C. J. Li, and J. P. Qi, "SHRIMP zircon U-Pb age of the gabbro dyke in the Luanchuan Pb-Zn-Ag orefield, east Qinling orogen and its constraint on mineralization time," *Acta Petrologica Sinica*, vol. 5, pp. 2951–2956, 2009.
- [65] J. J. Zhang and Y. D. Zheng, "The multiphase extension and their ages of the Xiaoqinling metamorphic core complex," *Acta Geologica Sinica*, vol. 73, pp. 139–147, 1999.
- [66] Q. Z. Shi, X. D. Wei, M. L. Li, and J. Q. Pang, *Nappe and Extensional Detachment Structures in North Side of East Qinling*, vol. 204, Geological Publishing House, Henan, Beijing, 2004.
- [67] J. S. Han, J. M. Yao, H. Y. Chen, X. H. Deng, and J. Y. Ding, "Fluid inclusion and stable isotope study of the Shagou Ag-Pb-Zn deposit, Luoning, Henan province, China: implications for the genesis of an orogenic lode Ag-Pb-Zn system," *Ore Geology Reviews*, vol. 62, pp. 199–210, 2014.
- [68] Z. J. Zhou, Y. J. Chen, S. Y. Jiang, H. X. Zhao, Y. Qin, and C. J. Hu, "Geology, geochemistry and ore genesis of the Wenyu gold deposit, Xiaoqinling gold field, Qinling Orogen, southern margin of North China Craton," *Ore Geology Reviews*, vol. 59, pp. 1–20, 2014.